applied sciences

MDPI

Article

Additive Manufacturing for Sensors: Piezoresistive Strain Gauge with Temperature Compensation

Anna Maria Lucia Lanzolla [1], Filippo Attivissimo [1], Gianluca Percoco [2], Mattia Alessandro Ragolia [1,*], Gianni Stano [2] and Attilio Di Nisio [1]

[1] Department of Electrical and Information Engineering, Polytechnic of Bari, 70126 Bari, Italy
[2] Department of Mechanics, Mathematics and Management, Polytechnic of Bari, 70126 Bari, Italy
* Correspondence: mattiaalessandro.ragolia@poliba.it

Featured Application: These sensors could be employed for collaborative robotic applications to interact with humans or delicate objects due to their possible integration into more complex devices in a single-step fabrication cycle.

Abstract: Additive manufacturing technologies allow the fabrication of smart objects, which are made up of a dielectric part and an embedded sensor able to give real-time feedback to the final user. This research presents the characterization of a low-cost 3D-printed strain sensor, fabricated using material extrusion (MeX) technology by using a conductive material composed of a polylactic acid (PLA)-based matrix doped with carbon black and carbon nanotubes (CNT), thus making the plastic conductive. A suitable measurement set-up was developed to perform automatic characterization tests using a high repeatability industrial robot to define either displacement or force profiles. The correlation between the applied stimulus and the variation of the electrical resistance of the 3D-printed sensor was evaluated, and an approach was developed to compensate for the effect of temperature. Results show that temperature and hysteresis affect repeatability; nevertheless, the sensor accurately detects impulse forces ranging from 10 g to 50 g. The sensor showed high linearity and exhibited a sensitivity of 0.077 $\Omega\ g^{-1}$ and 12.54 $\Omega\ mm^{-1}$ in the force and displacement range of 114 g and 0.7 mm, respectively, making them promising due to their low cost, ease of fabrication, and possible integration into more complex devices in a single-step fabrication cycle.

Keywords: additive manufacturing; fused filament fabrication; 3D printing; conductive materials; carbon nanotubes; sensors characterization; piezoresistive strain sensors; force sensors; robotic arm

Citation: Lanzolla, A.M.L.; Attivissimo, F.; Percoco, G.; Ragolia, M.A.; Stano, G.; Di Nisio, A. Additive Manufacturing for Sensors: Piezoresistive Strain Gauge with Temperature Compensation. *Appl. Sci.* **2022**, *12*, 8607. https://doi.org/10.3390/app12178607

Academic Editors: Longxing Su, Bingsheng Li and Kaike Yang

Received: 22 July 2022
Accepted: 25 August 2022
Published: 28 August 2022

1. Introduction

Additive manufacturing (AM), well known for being well suitable in different fields such as aerospace [1] and biomedical [2], has been gaining popularity for the fabrication of unconventional (i) non-assembly mechanisms [3], (ii) 4D printed structures [4], and (iii) metamaterials [5]. Recently, a new wave of 3D-printed structures is becoming appealing: the fabrication of smart objects with embedded sensors.

The key enabler for the fabrication of smart objects is the additive manufacturing of conductive materials used to create embedded sensing systems. Due to the possibility of extruding multiple materials simultaneously, AM seems to be the right technology to exploit for the fabrication of objects with embedded sensor systems [6].

In the case of fused filament fabrication (FFF) technology, piezoresistive materials can be exploited to fabricate sensors. Piezoresistivity describes the electrical resistivity change when a material is subjected to an external force. In order to exhibit piezoresistive properties, the FFF structure has to be electrically conductive. However, the extruded materials are usually thermoplastics. Therefore, they are not conductive. In this case,

materials are made conductive by doping a polymeric matrix with conductive particles (such as carbon nanotubes) [7].

The piezoresistive effect of nanocomposite materials is mainly due to (i) the inherent piezoresistivity of the conductive nanoparticles, (ii) the modification of inter-nanoparticle distances (affecting tunneling resistance between adjacent nanoparticles), and (iii) the deformation of conductive networks formed by nanoparticles within the polymer [8,9].

Kim et al. [10] developed a multiaxial sensor made up of a conductive material and a flexible thermoplastic polyurethane (TPU) to detect a change of force along three axes till 4 N.

Stano et al. [11] fabricated in a single step a smart load cell composed of TPU and four embedded strain gauges (conductive material): after connecting the strain gauges in a full Wheatstone bridge configuration, a sensitivity of 0.008 $\frac{\mathrm{mV}}{\mathrm{V\,g}}$ in the range [0, 100] g was found.

By tailoring a new 3D printing strategy, Alshaari et al. [12] fabricated, using a dual extruder machine, a porous sensor that can be easily integrated into biomedical devices (such as rehabilitative gloves) able to detect small applied pressure values. On the other hand, the authors pointed out a high viscoelastic effect due to the conductive plastic.

Another example of a smart object is provided in [13]; they manufactured and tested in a single step, a soft pneumatic network (Pneunet) actuator with an embedded piezoresistive sensor placed in the bottom of the structure able to provide feedback (change in resistance) when the actuator is pressurized.

A new promising field involving MeX technologies is the fabrication of an accelerometer [14,15]: in particular, in a range of [10, 50] $m\ s^{-2}$ excitation amplitude, a linear response has been found out. The possibility to reduce the current accelerometer size (37 mm $\times$ 37 mm $\times$ 37 mm) will enable the fabrication of small smart devices, which could potentially find application in the mechanic-electronic domain.

Another class of 3D-printed sensors that is a candidate to be widely exploited in the future is the capacitive ones: innovative capacitive sensors fabricated using FFF technology have been recently proposed for the detection of force, strain, and temperature [16–20].

Several process parameter studies have been performed to reduce the gap in knowledge about the reduction of 3D-printed sensors. Stano et al. [21] found the welding effect to be responsible for the increase in resistance and variability. The layer height and the total number of layers have to be reduced to reduce the aforementioned effect. Palmic et al. [22] found a mix of several parameters (nozzle temperature, layer height, space width, and bed temperature) to minimize the final electrical resistance in 3D-printed tracks. This way, the fabrication of embedded sensors will be easier and more reliable.

Post-processing treatments are another way to improve the final sensor conductivity. Flash metal ablation (FAM), a non-invasive technique, has been proven to improve the final conductance by two orders of magnitude by dissolving the superficial plastic and improving the bond among conductive fillers scattered into the conductive composite material [23].

Scientific literature has reported at different stages the strong dependence of 3D-printed sensors' performance by temperature [17,24–27], suggesting how the study of this effect and its compensation is crucial to push more the role of the AM for the fabrication of sensors.

In the present paper, we characterize the low-cost FFF strain sensors fabricated in [21] by performing a calibration to investigate the relationship between the resistance of the sensors and the applied force or displacement. We propose an approach to compensate for the influence of temperature, which strongly affects the electrical resistance, as highlighted in [27]. The obtained results are promising, considering the low cost, ease of fabrication of the proposed sensors, and the possibility of directly integrating them into more complex systems in one fabrication cycle.

2. Materials and Methods

2.1. Fabrication of the 3D-Printed Strain Sensor

The fused filament fabrication (FFF) technology has been used to manufacture in a single shot both the piezoresistive strain gauge and the dielectric support structure (Figure 1). The dual-extruder Ultimaker S5 (Ultimaker, Utrecht, The Netherlands) was exploited in conjunction with a soft material (polyurethane thermoplastic, henceforth TPU) and a conductive material (polylactic acid matrix doped with carbon nanotubes, henceforth CPLA). Thanks to the dual-extruder FFF machine, two filaments can be extruded in the same printing cycle (paper [28] provides a comprehensive review of the 3D printer set-up allowing multi-material extrusion on the market). As shown in scientific literature, the adhesion between the two materials is a crucial point. It depends on several factors such as materials affinity, chemical composition, and process parameters [29,30] which have been taken into account during the manufacturing process.

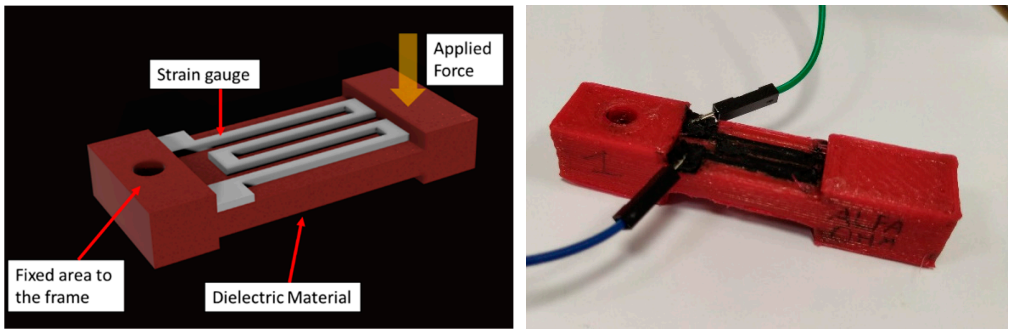

(**a**) (**b**)

Figure 1. (**a**) 3D model and (**b**) realization of the proposed strain sensor.

Two identical samples were manufactured: more details about the dimensions, the printing strategies, and the process parameters can be found in [21].

It is worth mentioning that the process parameters have been chosen to minimize the final electrical resistance and its variability, as shown in [21].

2.2. Experimental Set-Up

The experimental set-up is shown in Figure 2. It consists of:

1. An RV-2F-D industrial robot (Mitsubishi MELFA), with a spatial resolution of 0.01 mm along each axis and a repeatability of 0.02 mm. The robot is moved vertically to impress known force or displacement on the sensors and to allow repetitive experimental tests.
2. Two FFF sensors, fabricated by using the same production parameters: one sensor under test (S_a), which is pushed by the robot, and another dummy sensor (S_d), subject only to temperature variations and environmental factors. In this way, it is possible to evaluate the effect of temperature changes separately.
3. A load cell (500 g measurement range) to measure the force applied by the robot. A two-point calibration is performed on the load cell by employing calibrated weights before its use.
4. A thermocouple, placed near S_a; and two digital temperature sensors (Dallas DS18B20) with a resolution of 0.06 °C: one is placed near the dummy sensor (S_d), the other near the load cell.
5. Three GDM-8351 digital multimeters to measure the resistance of the two FFF sensors and thermocouple voltage.
6. A control unit was developed in LabVIEW to control the robot and the instruments and for data processing.

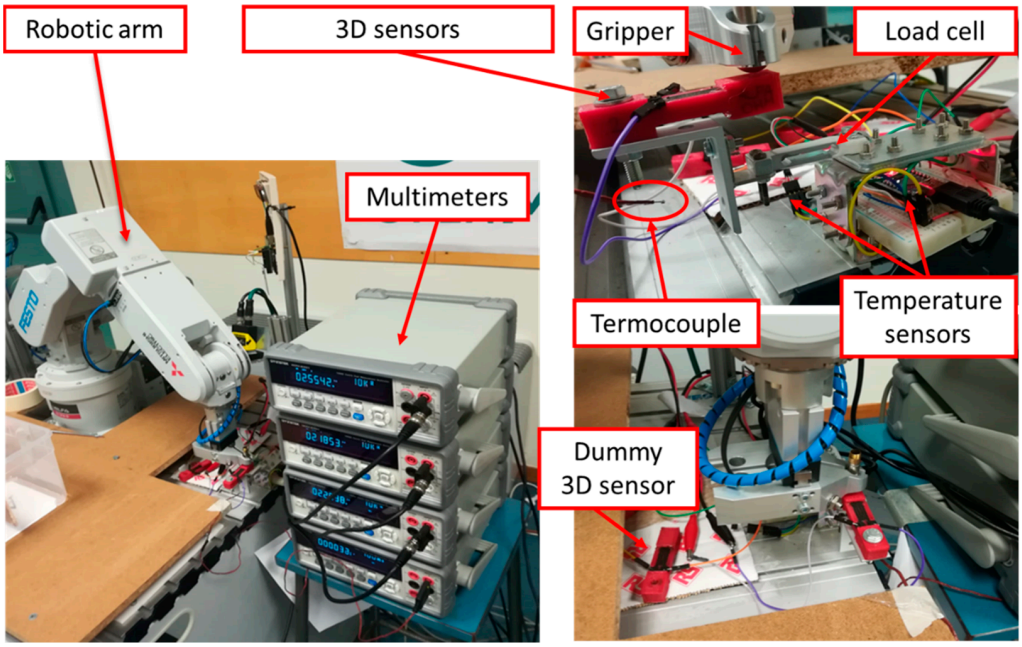

Figure 2. Experimental set-up.

The robot end-effector holds a rounded tip/head to touch one extremity of S_a and to apply a bending deformation. S_a, on the other extremity, is fixed on the load cell (through a metal structure), which measures the force applied on S_a. The variation of resistance of the load cell is converted using the XFW-HX711 module, which employs a high-precision 24-bit analog-to-digital converter (ADC), and the converted signal is acquired by an Arduino UNO board, which also acquires the temperature measured by the two digital temperature sensors. Each measured force value is the mean of 40 acquired load cell measurements. The number of repeated measurements has been chosen as a good compromise between noise reduction and data rate. The resistance of the FFF sensors is measured using the multimeters with a 2-wire configuration since the resistance of the FFF sensors is higher than 20 kΩ.

2.3. Calibration Tests

Several tests have been performed to obtain relations between sensor resistance, applied force and displacement. During the experiments, all those quantities have been continuously monitored while the robot is controlled to follow any one of the force or displacement profiles described in detail below and shown in Figure 3.

Before each calibration test, the robot is automatically placed in a contact position with the following procedure: a zeroing of the load cell is performed; then, the robot moves down towards S_a; when a force significantly higher than the standard deviation of load cell noise is measured, the robot moves up until the force is no longer detected.

Two preliminary tests, here named for reference as PF1 (Preliminary Force profile 1) and PF2, have been performed to observe the response of S_a, to quantify its sensitivity (ohm per gram), tune the proportional force control, and evaluate the effect of temperature. For that purpose, 0 g–10 g (test PF1) and 0 g–50 g (test PF2) cyclic on-off load profiles have been defined, with a corresponding displacement range of 0.1 mm and 0.4 mm, respectively. These two preliminary tests have led to identifying a step of 20 g as the minimum force step suitable for the following calibration tests (as explained in Section 3). Hence, three force/displacement profiles have been defined to calibrate S_a:

1. F1 (Force profile 1): it is composed of 5 cycles with a force range of 90 g, corresponding to a displacement range of about 0.6 mm. Each cycle is composed of the following steps: 0 g (relaxation step), then increasing force from 10 g (chosen as threshold value)

to 90 g with a step of 20 g (as obtained by the preliminary tests), then decreasing force down to 10 g, and finally 0 g. Each step has a duration of 3 min. Each relaxation step has a duration of 10 min. Since the actuation of the robot is in terms of position, proportional force control is performed by choosing a feedback control constant k_f = 0.0078 mm/g.

2. D1 (Displacement profile 1): in this case, the vertical position of the robot (instead of impressed force) is directly given as a function of time; hence the test is defined despite any change in the force-displacement relation and is unaffected by force control errors. The profile comprises 6 cycles with a displacement range of 0.7 mm, corresponding to about 114 g. The range and number of cycles have been slightly increased with respect to the previous profile to ensure to cover the whole previous force range despite possible changes in material behavior due to viscoelasticity and the Mullins effect [17]. Each cycle is composed of the following steps: from 0 mm (no load) to 0.7 mm (maximum load), then back to 0 mm, with steps of 0.1 mm (corresponding to about 20 g). Each step lasts 3 min (49 min per cycle). The no-load step between two consecutive cycles has a duration of 10 min. During this test, the set-up was changed: a cardboard barrier was placed around the test area to make it less sensitive to temperature variations.
3. D2 (Displacement profile 2): in order to validate the obtained results, we decided to calibrate the sensor by defining a longer calibration test, composed of 12 cycles (force range of about 114 g, displacement range of 0.7 mm), to verify if the number of performed test cycles affects the results due to material softening. As in Test D1, each cycle is composed of the following steps: from 0 mm (no load) to 0.7 mm (maximum load), then back to 0 mm, with a step of 0.1 mm. Each step has a longer duration of 5 min (75 min per cycle) to allow the mechanical settling of S_a and the force to stabilize. The no-load step between two consecutive cycles has a duration of 10 min. The 12 cycles are divided into two subsets of 6 cycles, separated with a no-load step of 60 min, to evaluate for possible material recovery from stress. During this test, the set-up was furtherly changed: the test area was completely covered with a plastic barrier to isolate the set-up from the environment completely.

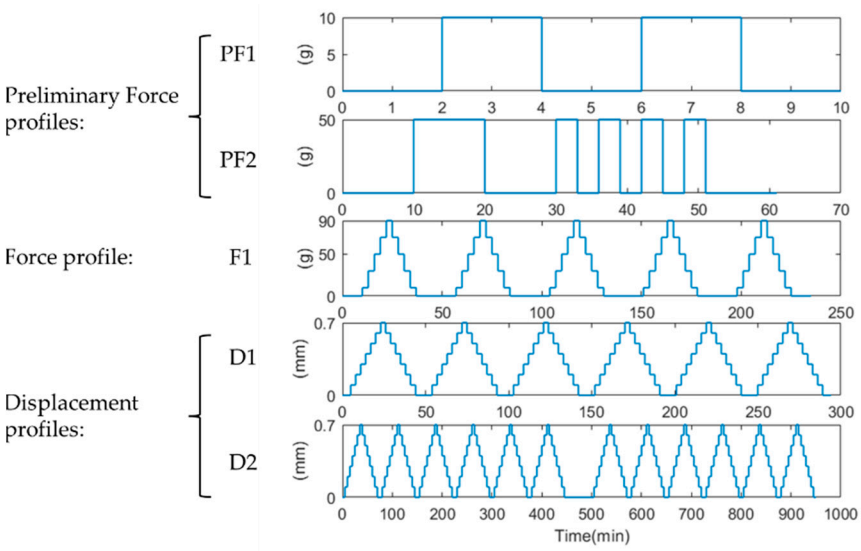

Figure 3. From top to bottom: two preliminary force profiles (PF1 and PF2), Force profile 1 (F1), Displacement profile 1 (D1), and Displacement profile 2 (D2).

2.4. Data Analysis

2.4.1. Data Segmentation

To correctly calibrate S_a, only data related to steady states should be considered, thus removing transient states from the force/displacement stepped profiles. Hence, a binary

segmentation is performed on measured force/displacement data to separate transient states and steady states, and a labeling operation on the identified steady states is carried out. The segmentation is performed by computing the centered moving SD (standard deviation) of the input data, with a size of 11 samples, thus selecting as 'steady' all those points with an SD below a defined threshold (dependent on the force or displacement profile). Then, a morphological opening (i.e., an erosion followed by dilation) with a linear kernel of size 6 samples is applied to the binary array to remove the outliers. A label is assigned to each identified steady state. All following analyses are applied only to labeled signal portions, i.e., excluding transient states.

2.4.2. Repeatability

Sensor intrinsic repeatability between consecutive cycles was calculated by considering resistance measurements $\overline{R}_{ij}$, indexed by test cycle $j = 1, \ldots, n$ (where n is the number of cycles), and step $i = 1, \ldots, \mathrm{n_T}$ (where n_T is the number of defined steps). Each $\overline{R}_{ij}$ has been calculated as the mean of measurements of the labeled signal portion corresponding to that cycle and step (i.e., when force and resistance are stable) to reduce noise. Therefore, repeatability has been calculated as follows:

$$r = \underset{i}{\mathrm{mean}}\left(\underset{j}{\mathrm{std}}\ \overline{R}_{ij}\right) i = 1, \ldots, n_T \quad j = 1, \ldots, n$$

where standard deviations are evaluated in sets corresponding to the same step and different cycles.

2.4.3. Temperature Compensation

The effect of temperature on the electrical resistance R_a of the sensor S_a must be compensated to obtain an accurate force or displacement measurements.

The following temperature compensation approach has been developed for this purpose: the compensated resistance R_c can be obtained as:

$$R_c = R_a - f(G) \tag{1}$$

where G is a reference variable (e.g., a measured temperature or the resistance of the dummy sensor) and $f(G) = \sum_{i=0}^{N} c_i G^i$ is a polynomial of degree $N = 3$, since preliminary tests showed a nonlinear relationship. In some cases, the degree of the polynomial can be reduced to $N = 1$ or 2 if the results are comparable.

$f(G)$ describes the relationship between R_a and the reference variable G when S_a is not stressed (i.e., only considering no-load steps), allowing to separate and compensate for the effect of temperature on R_a. Indeed, the coefficients c_i are obtained with Ordinary Least Squares (OLS) fitting of $f(G)$ over R_a measured when force and displacement are zero.

Each temperature sensor and the dummy sensor have been considered in turn as reference variables G, and the repeatability r defined in Section 2.4.2 has been applied to R_c and has been used to choose the reference variable G and the polynomial order.

Then, a second polynomial (up to the 3rd degree, which can be reduced to the 1st or 2nd degree as for Equation (1)), is used for fitting the relationship

$$F = f_F(R_c) \text{ or } P = f_P(R_c) \tag{2}$$

between the measured applied force F (or the displacement P applied by the robot) and R_c, by considering all performed cycles, the results are evaluated through the repeatability r and the RMSE of the fitting.

3. Results

For each test, regardless of the type of profile (force or displacement), the analysis is performed by calibrating with respect to both force and to displacement, i.e., by finding

both polynomials f_F and f_P. This is to assess whether better results are obtained with force or displacement and if this correlates with the profile type.

3.1. On-Off Preliminary Force Tests PF1 and PF2 (Ranges of 10 g, 0.1 mm, and 50 g, 0.4 mm, Respectively)

Figure 4 shows the results of resistance compensation on the preliminary on-off tests performed to obtain a first estimate of sensor sensitivity (ohm per gram) and to evaluate the influence of temperature. The high correlation between temperature T_2 and resistances R_a and R_d is clear in Figure 4. Moreover, the variation of R_a due to the 10 g steps in test PF1 is not distinguishable from the variation due to temperature (Figure 4c), whereas the 50 g steps are better observable even in the presence of temperature drift due to their higher amplitude (Figure 4h). Hence, temperature compensation is performed with respect to R_d for test PF1 and test PF2. Force reconstruction led to an RMSE of 3.0% in the 50 g range, whereas an RMSE of 17.3% is obtained in the 10 g range. However, the absolute RMSE values are comparable, with values of 1.5 g and 1.7 g for tests PF1 and PF2, respectively. The RMSE results obtained in both cases prove that the compensation procedure with the proposed method allows reconstructing the force applied on S_a, which results in being very sensitive to 50 g steps with good accuracy, but it can also discriminate 10 g steps. The experimental results led to the choice of 20 g steps for the following force profile as a trade-off between the total number of steps (and test time) for a given range and the expected capability of clearly observing force changes.

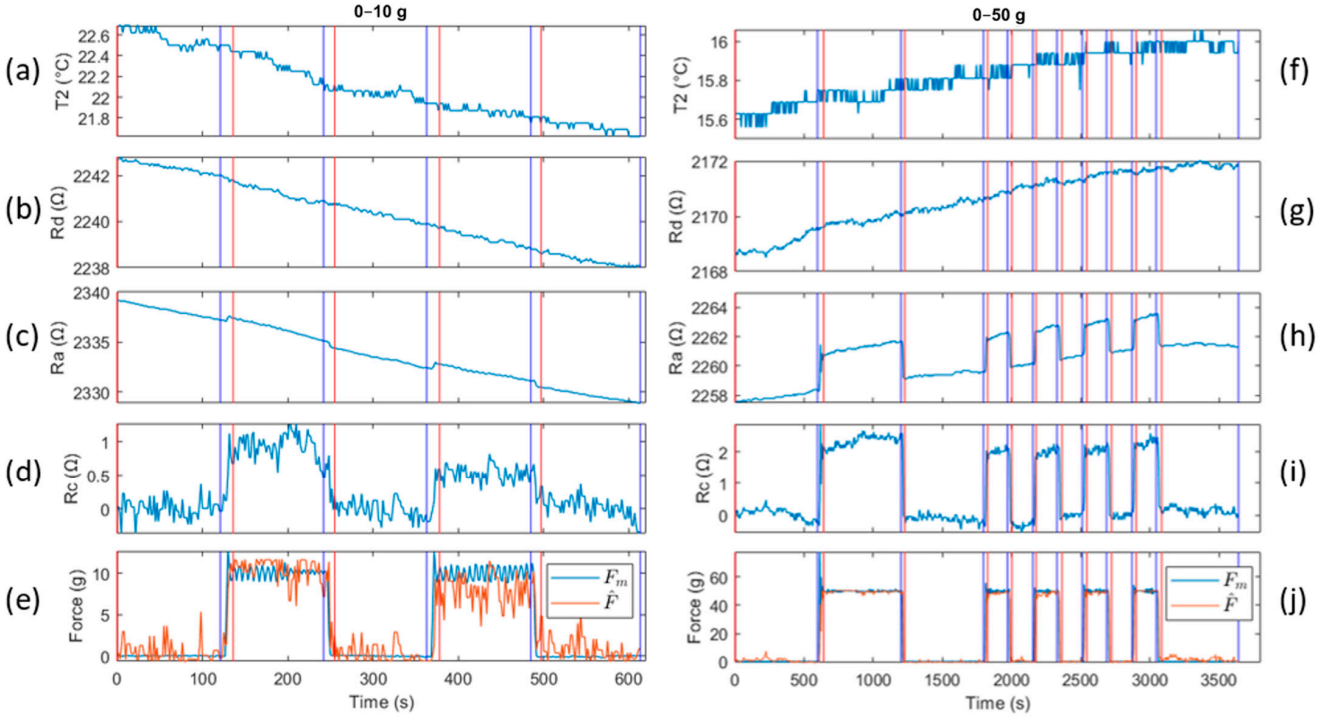

Figure 4. Preliminary on-off tests PF1 and PF2. From top to bottom: the digital temperature sensor (T_2), the resistance of the dummy sensor (R_d), the resistance of the sensor under test before (R_a) and after (R_c) compensation, and measured (F_m) and fitted ($\hat{F}$) force. Each label's beginning and end are a red and a blue vertical line, respectively. The 0–10 g test PF1 (**a**–**e**) has 5 labels, whereas the 0–50 g test PF2 (**f**–**j**) has 11 labels.

3.2. F1: Force Profile of 5 Cycles (Range: 90 g, 0.6 mm)

Fifty-one labels are identified through segmentation for test F1, where a force profile with 20 g steps was defined in a 90 g range by performing a feedback control loop with a proportional constant of 0.0078 mm/g. The temperature range during the test has been about 3.7 °C. Table 1 shows that R_a has the highest correlation with R_d. Regarding the re-

maining references, a better correlation is shown with the digital temperature sensors with respect to the thermocouple. This is probably due to different thermal inertia phenomena: the digital sensors are covered with a case, resulting in more similar to the FFF sensors (it somehow acts as the TPU structure of the FFF sensors, with a slower response to temperature changes), whereas the thermocouple is more directly exposed to fast temperature variations. Therefore, using the dummy sensor is well motivated and reduces any behavior differences that may occur when employing commercial temperature sensors.

Table 1. Pearson correlation coefficients with respect to R_a.

Test	R_d	T1	T2	TC
F1	0.8407	0.5456	0.7221	0.3695
D1	0.9192	0.8934	0.9135	0.6045
D2	0.9938	0.9753	0.9717	0.7585

The presence of hysteresis introduces errors during the compensation procedure. Hence, to reduce this effect, three calibrations are performed for both force and displacement by considering (i) only the increasing trait of each cycle, then (ii) only the decreasing trait, and finally (iii) the whole cycle.

The results obtained by applying temperature compensation are given in Table 2 for the calibration of force and Table 3 for the calibration of displacement, showing similar performance. Worst case, RMSE and r are 13.5% and 9.1% of the considered range, respectively. The performance metrics slightly improved when considering only the decreasing trait of the cycles.

By comparing different cycles, it has been observed that the robot elongation increases for increasing cycle index, which is more evident for higher forces. This is probably due to viscoelasticity and relaxation phenomena: the TPU structure slightly relaxes when the force step is applied repeatedly, thus becoming more flexible and opposing less mechanical resistance to the applied stress; hence, the force measured by the load cell decreases, and the robot moves furtherly to apply the desired force. Since this is common to all tests, the relationship between displacement and force change will be shown only in the discussion of test D2 for brevity.

Table 2. Comparison of results obtained for the three tests by applying the proposed temperature compensation approach based on dummy sensor resistance R_d. Calibration is with respect to force. Values are expressed as a percentage of the range.

Trait	Metric	Test F1	Test D1	Test D2		
				1st Series	2nd Series	All Cycles
Increasing	RMSE	11.6	8.4	4.5	9.8	11.4
	r	8.4	4.8	3.9	6.9	10.4
Decreasing	RMSE	9.5	3.3	4.9	7.5	13.2
	r	8.3	2.2	4.6	6.4	11.7
Whole cycle	RMSE	12.1	9.2	6.9	10.2	13.2
	r	9.1	3.7	4.5	7.6	10.8

Table 3. Comparison of results obtained for the three tests by applying the proposed temperature compensation approach based on dummy sensor resistance R_d. Calibration is with respect to displacement. Values are expressed as a percentage of the range.

Trait	Metric	Test F1	Test D1	Test D2		
				1st Series	2nd Series	All Cycles
Increasing	RMSE	13.5	7.9	6.3	11.9	12.5
	r	9.1	4.9	4.1	7.2	10.3
Decreasing	RMSE	11.8	7.3	5.6	8.1	13.6
	r	7.7	3.0	4.4	6.4	11.7
Whole cycle	RMSE	13.1	9.8	6.8	12.0	13.7
	r	9.0	4.6	4.4	8.1	11.0

3.3. D1: Displacement Profile of 6 Cycles (Range: 0.7 mm, 114 g)

Eighty-five labels are identified through segmentation for test D1, where a displacement profile with 0.1 mm steps is defined in a 0.7 mm range. The temperature range during the test has been about 3.5 °C. To focus on temperature compensation and reduce the effects of viscoelasticity, measurements relevant to the first cycle have been discarded. The total number of cycles has been increased by one with respect to test F1.

Table 1 shows that R_a has the highest correlation with the resistance R_d of the dummy sensor. Overall, R_a correlates better with all quantities with respect to test F1, and correlations with the digital temperature sensors increase and reach values similar to the dummy sensor: this is probably due to the isolation provided by the cardboard.

Compensation has been calculated by using a dummy sensor resistance R_1. Again, increasing and decreasing traits are first analyzed separately to investigate the effect of hysteresis.

The results in Tables 2 and 3 show, in general, no significant differences when calibrating with respect to force than to displacement, with worst case RMSE and r of 9.8% and 4.9% of the considered range, respectively. The best results are obtained when considering the decreasing traits of the calibration with respect to force, where RMSE and r are 3.3% and 2.2%, respectively.

3.4. D2: Displacement Profile of 12 Cycles (Range: 0.7 mm, 114 g)

One hundred sixty-nine labels are identified through segmentation for test D2, composed of two series of 6 cycles following the strain profile of test D1 with a longer step duration and with a long pause of 60 min between the two series. The temperature range during the test was about 7.2 °C considering all cycles, 5.4 °C for the first six cycles, and 5.0 °C for the last six cycles, and R_a showed the highest correlation with R_d (Table 1). As in test D1, the correlation with the digital temperature sensors increases and reaches a value comparable to the dummy sensor due to the isolation provided by the plastic barrier.

Three data elaborations are performed: (i) on the first series of cycles, (ii) on the second series of cycles, (iii) on both series of cycles. In all cases, the first cycle has been excluded from fitting to focus on compensation rather than viscoelasticity, as done in the previous test.

Figure 5f shows the resistance R_c after temperature compensation is applied to the first series of cycles, the effect of temperature is mitigated, and the force/displacement is reconstructed (Figure 5g) by fitting a 1st-degree polynomial since 3rd- and 2nd-degree polynomials led to comparable results. No significant differences are found when calibrating with respect to force than displacement, as can be observed in Figure 5g. When considering only one series, the performance metrics improve, particularly for the first series, where RMSE and r are lower than 6.9% and 4.6% of the considered range, respectively, when applying temperature compensation (Tables 2 and 3). This could be explained by observing Figure 5a, where the temperature change for the first series is monotonous, whereas it rapidly increases for the last two cycles of the second series. This indicates that when

temperature variation is slow and monotonous, its compensation is easier to be performed, and small force steps can be easily detected and measured with better accuracy. This behavior suggests that the performance of temperature compensation should be verified in conditions similar to the target application.

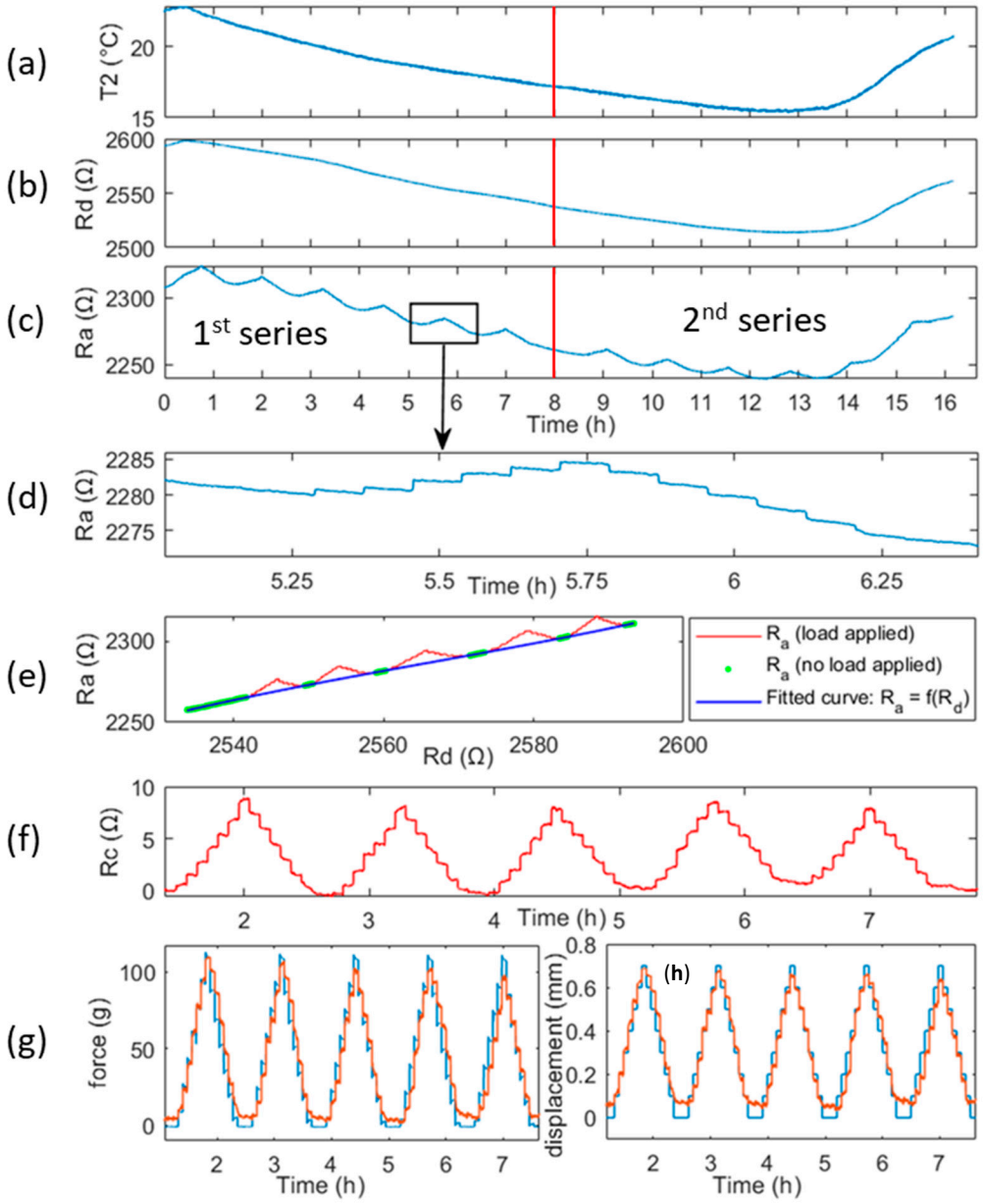

Figure 5. From top to bottom: (**a**–**d**) T_2, R_d, R_a, and R_a detail vs. time; (**e**) R_a vs. R_d, and performed fitting $R_a = f(R_d)$; (**f**) R_c vs. time (2nd to 6th cycle); force (**g**) and displacement (**h**) vs. time, after temperature compensation (true and estimated values are in blue and red, respectively). All data are referred to as test D2. Temperature compensation and force or displacement reconstruction are done with respect to the 1st series of cycles.

Again, as observed in test D1, the force for a given displacement decreases as long as the test proceeds from cycle to cycle, which is clearly shown in Figure 6. It can be seen that the largest difference, of about 6 g, is between the first and the second cycle and becomes smaller subsequently. Hence, the first cycle has been discarded from calibration data. Moreover, during each step in which the displacement is held constant, it is observed that force can decrease up to 3 g. Within each cycle, multiple force values are measured at

the same displacement step due to the force settling time caused by the viscoelasticity of the TPU structure.

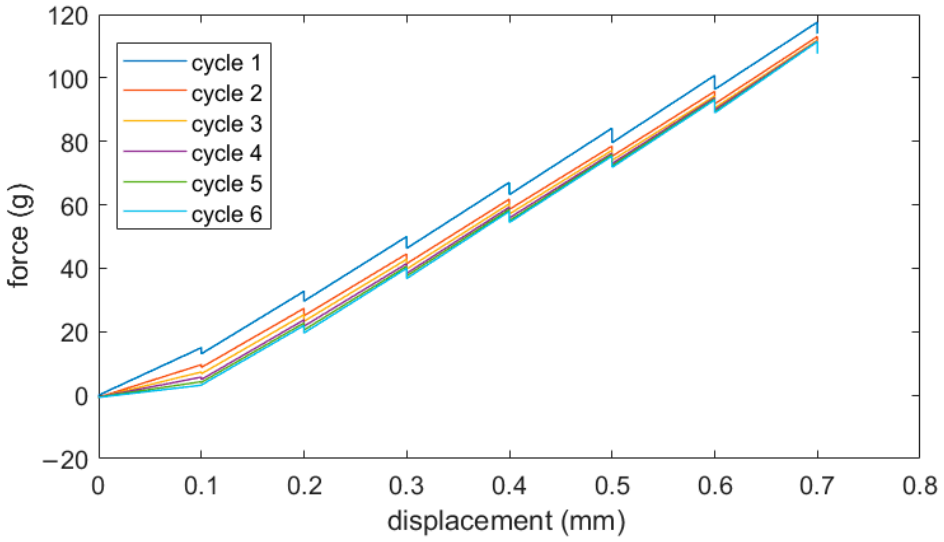

Figure 6. Applied force vs. displacement, considering the increasing traits of the 1st series of cycles of test D2. For increasing cycle index, the force reduces for a given strain, and this gap is higher than the 1st cycle, which is excluded from the analysis. Moreover, within each cycle, multiple force values are measured at the same displacement step due to the force settling time caused by the viscoelasticity of the TPU structure. Since strain changes in steps of 0.1 mm, the force between steps is linearly interpolated in the plot.

4. Discussion

Temperature highly affects the resistance of the FFF sensors, causing resistance variations up to 12 Ω/°C. The temperature was not controlled during experiments to make it vary (reaching a range of 7.2 °C, with a maximum slope of 4.4 °C/h), thus analyzing a variation of properties due to temperature and finding a model to suitably describe this relationship. Covering the experimental set-up to reduce rapid temperature changes and provide uniform temperature conditions inside the test area allowed better results in terms of temperature compensation. In particular, using a dummy sensor as a reference for temperature compensation proved more effective than using temperature sensors since the dummy sensor exhibits the same response to temperature changes as the sensor under test. Moreover, we observed that slow and monotonous temperature variations led to enhanced temperature compensation, improving the accuracy of force estimation. In contrast, fast and sudden temperature variations (e.g., variation of the slope sign) reduced the compensation results. This is probably related to the dynamic behavior of the material, as well as to hysteresis when the slope of the temperature signal changes sign. Hence, the tests should be performed in conditions similar to the target application to obtain reproducible performance. It should be noted that a temperature increase may arise if the sensor is solicited with higher forces or elongations and with faster loading cycles. This is common behavior of many polymers, such as polyethylene [31], and has been studied, for bulk TPU, in [32], where higher stress and strain levels have been applied with respect to the ones considered in this paper.

The best performance metrics (RMSE = 6.9% and r = 4.5% of the force range, and RMSE = 6.8% and r = 4.4% of the displacement range) are obtained when considering the first series of cycles of test D2 and excluding the first cycle: this generally improves results, since during the first cycle the sensor under test is in a settling phase. This is common behavior of polymer materials such as TPU and doped polymers such as PLA doped with CNT, which exhibit phenomena of viscoelasticity, a combination of permanent and recoverable changes, and the Mullins effect [33,34]. Modeling these effects is difficult

since the results depend on time-varying stress and strain, on material fabrication, and the proposed sensor may also depend on the interaction between the TPU substrate and the conductive PLA.

Calibration with respect to force and displacement led to similar results. For the first series of cycles of test D2 (which led to the best performance metrics), the following linear relationship was found between applied force and compensated resistance (3rd and 2nd-degree polynomials led to comparable results):

$$F = f(R_c) = a_1 R_c + a_2 \tag{3}$$

where $a_1 = 13.05$ g Ω^{-1} and $a_2 = 1.96$ g, and R_c is obtained as a function of R_1 with a cubic relationship:

$$R_c = R_a - \left(b_1 R_d^3 + b_2 R_d^2 + b_3 R_d + b_4\right) \tag{4}$$

where $b_1 = 7.3941 \cdot 10^{-5}\ \Omega^{-2}$, $b_2 = -0.5693\ \Omega^{-1}$, $b_3 = 1461.6641$, and $b_4 = -129465.2842\ \Omega$. The metric r for Equation (4) is 4.5% of the range of the compensated resistance R_c.

Hence, the sensitivity of the sensor under test is $s = 1/a_1 = 0.077\ \Omega\ \mathrm{g}^{-1}$ and estimation of resistance change due to the displacement along the vertical axis can be calculated as $\Delta R/\Delta L = 12.54\ \Omega\mathrm{mm}^{-1}$ by considering force and displacement ranges of 114 g and 0.7 mm, respectively. This means that if temperature affects resistance up to 12 $\Omega/^{\circ}$C, then a variation ΔT = 0.1 °C can lead to a displacement measurement error of 0.1 mm or a force measurement error of 15 g:

$$e_d = \frac{0.1\ ^{\circ}\mathrm{C} \cdot 12\ \frac{\Omega}{^{\circ}\mathrm{C}}}{12.54\ \Omega\mathrm{mm}^{-1}} \cong 0.1\ \mathrm{mm}\ e_f = \frac{0.1\ ^{\circ}\mathrm{C} \cdot 12\ \frac{\Omega}{^{\circ}\mathrm{C}}}{0.077\ \Omega\mathrm{g}^{-1}} \cong 15\ \mathrm{g} \tag{5}$$

Hence temperature compensation is crucial, particularly when small force steps are considered.

Overall, the presence of hysteresis affects calibration results of all tests, with absolute values five times higher with respect to the preliminary on-off tests PF1 and PF2, where no hysteresis was present but still obtained RMSE lower than 13% of the tested range. This suggests that good accuracy can be achieved when employing this kind of sensor to detect impulse forces or the presence of a load.

In the present paper, low-cost 3D printed strain gauges have been characterized to reduce the gap in knowledge found in the scientific literature. A way to compensate for the temperature effect when the sensor is employed for force measurement was found and discussed. Several studies have been conducted in the past few years to correlate process parameters to sensor performances to enhance these latter. Indeed, since the fabrication process is at an early stage and constantly evolving, particular efforts should be focused on the choice of extruded materials. A new challenge, from a manufacturing standpoint, is using new material extrusion techniques based on the deposition of conductive inks in conjunction with thermoplastic material extrusion to level up sensor performances and push the role of AM technologies in the field of sensor fabrication.

5. Conclusions

The possibility of manufacturing smart objects is very appealing, reducing time, cost, and assembly tasks. Additive manufacturing (AM) technologies seem to be the key enabler to achieve this goal, and several fields, like the biomedical one, can take full advantage from smart devices. Fused filament fabrication (FFF) is the most inexpensive AM technology. It has recently been employed to manufacture smart objects with embedded sensors in a single-step fabrication cycle. This research presents the characterization of a low-cost 3D-printed strain sensor fabricated using FFF technology by using a commercial conductive material composed of a polylactic acid (PLA)-based filament doped with carbon black and carbon nanotubes (CNT). A high repeatability industrial robot was used to perform

automatic tests, following suitable force/displacement profiles. The sensor exhibited a sensitivity of 0.077 $\Omega\ g^{-1}$ and 12.54 $\Omega\ mm^{-1}$.

Since sensor resistance also depends strongly on temperature, a compensation method was developed based on the resistance change of an unsolicited dummy sensor. The method proved effective; however, experimentation revealed the presence of nonnegligible sensor hysteresis and material viscoelasticity that will be the object of further investigation.

Overall, for two-step profiles (on-off), the reconstruction of the applied force/displacement led to acceptable performances. This suggests the suitability of these sensors to detect impulse forces or the presence of a load. For instance, they could be employed for collaborative robotic applications to interact with humans or delicate objects since the FFF process allows directly integrating these sensors into more complex objects in one single fabrication cycle and adjusting to the shape of the fabricated smart structure.

Author Contributions: Conceptualization, M.A.R. and G.S.; Methodology, A.M.L.L., F.A., G.P. and A.D.N.; Supervision, A.M.L.L. and F.A.; Validation, M.A.R. and G.S.; Writing—original draft, M.A.R. All authors have read and agreed to the published version of the manuscript.

Funding: This research received no external funding.

Data Availability Statement: Data are contained within the article.

Conflicts of Interest: The authors declare no conflict of interest.

References

1. Blakey-Milner, B.; Gradl, P.; Snedden, G.; Brooks, M.; Pitot, J.; Lopez, E.; Leary, M.; Berto, F.; du Plessis, A. Metal additive manufacturing in aerospace: A review. *Mater. Des.* **2021**, *209*, 110008. [CrossRef]
2. Kumar, R.; Kumar, M.; Chohan, J.S. The role of additive manufacturing for biomedical applications: A critical review. *J. Manuf. Process.* **2021**, *64*, 828–850. [CrossRef]
3. Lussenburg, K.; Sakes, A.; Breedveld, P. Design of non-assembly mechanisms: A state-of-the-art review. *Addit. Manuf.* **2021**, *39*, 101846. [CrossRef]
4. Kumar, S.; Singh, R.; Batish, A.; Singh, T. Additive manufacturing of smart materials exhibiting 4-D properties: A state of art review. *J. Thermoplast. Compos. Mater.* **2022**, *35*, 1358–1381. [CrossRef]
5. Askari, M.; Hutchins, D.A.; Thomas, P.J.; Astolfi, L.; Watson, R.L.; Abdi, M.; Ricci, M.; Laureti, S.; Nie, L.; Freear, S.; et al. Additive manufacturing of metamaterials: A review. *Addit. Manuf.* **2020**, *36*, 101562. [CrossRef]
6. Schouten, M.; Wolterink, G.; Dijkshoorn, A.; Kosmas, D.; Stramigioli, S.; Krijnen, G. A Review of Extrusion-Based 3D Printing for the Fabrication of Electro- and Biomechanical Sensors. *IEEE Sens. J.* **2021**, *21*, 12900–12912. [CrossRef]
7. Arh, M.; Slavič, J.; Boltežar, M. Experimental identification of the dynamic piezoresistivity of fused-filament-fabricated structures. *Addit. Manuf.* **2020**, *36*, 101493. [CrossRef]
8. Dul, S.; Pegoretti, A.; Fambri, L. Fused Filament Fabrication of Piezoresistive Carbon Nanotubes Nanocomposites for Strain Monitoring. *Front. Mater.* **2020**, *7*, 12. [CrossRef]
9. Haghgoo, M.; Hassanzadeh-Aghdam, M.K.; Ansari, R. A comprehensive evaluation of piezoresistive response and percolation behavior of multiscale polymer-based nanocomposites. *Compos. Part A Appl. Sci. Manuf.* **2020**, *130*, 105735. [CrossRef]
10. Kim, K.; Park, J.; Suh, J.; Kim, M.; Jeong, Y.; Park, I. 3D printing of multiaxial force sensors using carbon nanotube (CNT)/thermoplastic polyurethane (TPU) filaments. *Sens. Actuators A Phys.* **2017**, *263*, 493–500. [CrossRef]
11. Stano, G.; di Nisio, A.; Lanzolla, A.; Percoco, G. Additive manufacturing and characterization of a load cell with embedded strain gauges. *Precis. Eng.* **2020**, *62*, 113–120. [CrossRef]
12. Alsharari, M.; Chen, B.; Shu, W. Sacrificial 3D Printing of Highly Porous, Soft Pressure Sensors. *Adv. Electron. Mater.* **2022**, *8*, 2100597. [CrossRef]
13. Singh, D.; Tawk, C.; Mutlu, R.; Sariyildiz, E.; Sencadas, V.; Alici, G. A 3D Printed Soft Force Sensor for Soft Haptics. In Proceedings of the 2020 3rd IEEE International Conference on Soft Robotics (RoboSoft), New Haven, CT, USA, 15 May–15 July 2020; pp. 458–463. [CrossRef]
14. Arh, M.; Slavič, J.; Boltežar, M. Design principles for a single-process 3d-printed accelerometer–theory and experiment. *Mech. Syst. Signal Process.* **2021**, *152*, 107475. [CrossRef]
15. Arh, M.; Slavič, J. Single-Process 3D-Printed Triaxial Accelerometer. *Adv. Mater. Technol.* **2022**, *7*, 2101321. [CrossRef]
16. Saari, M.; Xia, B.; Cox, B.; Krueger, P.S.; Cohen, A.L.; Richer, E. Fabrication and Analysis of a Composite 3D Printed Capacitive Force Sensor. *3D Print. Addit. Manuf.* **2016**, *3*, 136–141. [CrossRef]
17. Ragolia, M.A.; Lanzolla, A.M.L.; Percoco, G.; Stano, G.; di Nisio, A. Thermal Characterization of New 3D-Printed Bendable, Coplanar Capacitive Sensors. *Sensors* **2021**, *21*, 6324. [CrossRef]

18. Schouten, M.; Sanders, R.; Krijnen, G. 3D printed flexible capacitive force sensor with a simple micro-controller based readout. In Proceedings of the 2017 IEEE Sensors Conference, Glasgow, UK, 29 October–1 November 2017; pp. 1–3. [CrossRef]
19. Loh, L.Y.W.; Gupta, U.; Wang, Y.; Foo, C.C.; Zhu, J.; Lu, W.F. 3D Printed Metamaterial Capacitive Sensing Array for Universal Jamming Gripper and Human Joint Wearables. *Adv. Eng. Mater.* **2021**, *23*, 2001082. [CrossRef]
20. Santiago, C.C.; Randall-Posey, C.; Popa, A.-A.; Duggen, L.; Vuksanovich, B.; Cortes, P.; Macdonald, E. Corrections to '3D Printed Elastomeric Lattices With Embedded Deformation Sensing'. *IEEE Access* **2020**, *8*, 87184. [CrossRef]
21. Stano, G.; di Nisio, A.; Lanzolla, A.M.; Ragolia, M.; Percoco, G. Fused filament fabrication of commercial conductive filaments: Experimental study on the process parameters aimed at the minimization, repeatability and thermal characterization of electrical resistance. *Int. J. Adv. Manuf. Technol.* **2020**, *111*, 2971–2986. [CrossRef]
22. Palmić, T.B.; Slavič, J.; Boltežar, M. Process Parameters for FFF 3D-Printed Conductors for Applications in Sensors. *Sensors* **2020**, *20*, 4542. [CrossRef]
23. Cardenas, J.A.; Tsang, H.; Tong, H.; Abuzaid, H.; Price, K.; Cruz, M.A.; Wiley, B.J.; Franklin, A.D.; Lazarus, N. Flash ablation metallization of conductive thermoplastics. *Addit. Manuf.* **2020**, *36*, 101409. [CrossRef]
24. Daniel, F.; Patoary, N.H.; Moore, A.L.; Weiss, L.; Radadia, A.D. Temperature-dependent electrical resistance of conductive polylactic acid filament for fused deposition modeling. *Int. J. Adv. Manuf. Technol.* **2018**, *99*, 1215–1224. [CrossRef]
25. Kwok, S.W.; Goh, K.H.H.; Tan, Z.D.; Tan, S.T.M.; Tjiu, W.W.; Soh, J.Y.; Ng, Z.J.G.; Chan, Y.Z.; Hui, H.K.; Goh, K.E.J. Electrically conductive filament for 3D-printed circuits and sensors. *Appl. Mater. Today* **2017**, *9*, 167–175. [CrossRef]
26. Király, A.; Ronkay, F. Temperature dependence of electrical properties in conductive polymer composites. *Polym. Test.* **2015**, *43*, 154–162. [CrossRef]
27. Ragolia, M.A.; di Nisio, A.; Lanzolla, A.M.; Percoco, G.; Scarpetta, M.; Stano, G. Thermal Characterization of Electrical Resistance of 3D printed sensors. In Proceedings of the 2021 IEEE International Instrumentation and Measurement Technology Conference (I2MTC), Glasgow, UK, 17–20 May 2021; pp. 1–6. [CrossRef]
28. Maurel, A.; Haukka, M.; MacDonald, E.; Kivijärvi, L.; Lahtinen, E.; Kim, H.; Armand, M.; Cayla, A.; Jamali, A.; Grugeon, S.; et al. Considering lithium-ion battery 3D-printing via thermoplastic material extrusion and polymer powder bed fusion. *Addit. Manuf.* **2021**, *37*, 101651. [CrossRef]
29. Lopes, L.R.; Silva, A.F.; Carneiro, O.S. Multi-material 3D printing: The relevance of materials affinity on the boundary interface performance. *Addit. Manuf.* **2018**, *23*, 45–52. [CrossRef]
30. Tamburrino, F.; Graziosi, S.; Bordegoni, M. The influence of slicing parameters on the multi-material adhesion mechanisms of FDM printed parts: An exploratory study. *Virtual Phys. Prototyp.* **2019**, *14*, 316–332. [CrossRef]
31. Avanzini, A. Effect of cyclic strain on the mechanical behavior of virgin ultra-high molecular weight polyethylene. *J. Mech. Behav. Biomed. Mater.* **2011**, *4*, 1242–1256. [CrossRef]
32. Avanzini, A.; Gallina, D. Effect of Cyclic Strain on the Mechanical Behavior of a Thermoplastic Polyurethane. *J. Eng. Mater. Technol.* **2011**, *133*, 021005. [CrossRef]
33. Guedes, R.M.; Singh, A.; Pinto, V. Viscoelastic modelling of creep and stress relaxation behaviour in PLA-PCL fibres. *Fibers Polym.* **2017**, *18*, 2443–2453. [CrossRef]
34. Pelayo, F.; Blanco, D.; Fernández, P.; González, J.; Beltrán, N. Viscoelastic Behaviour of Flexible Thermoplastic Polyurethane Additively Manufactured Parts: Influence of Inner-Structure Design Factors. *Polymers* **2021**, *13*, 2365. [CrossRef] [PubMed]